Research Article | Vol. 30, No. 17 / 15 Aug 2022 / Optics Express 30331
Optics EXPRESS

Temporal and spectral multiplexing for EUV multibeam ptychography with a high harmonic light source

NATHAN J. BROOKS,[1,4,*] BIN WANG,[1,4] IONA BINNIE,[1] MICHAEL TANKSALVALA,[1] YUKA ESASHI,[1] JOSHUA L. KNOBLOCH,[1] QUYNH L. D. NGUYEN,[1] BRENDAN MCBENNETT,[1] NICHOLAS W. JENKINS,[1] GUAN GUI,[1] ZHE ZHANG,[2] HENRY C. KAPTEYN,[1] MARGARET M. MURNANE,[1] AND CHARLES S. BEVIS[1,3]

[1]*STROBE Science and Technology Center, JILA, University of Colorado Boulder, Boulder, CO 80309, USA*
[2]*MOE Key Laboratory of Advanced Microstructural Materials, Institute of Precision Optical Engineering, School of Physics Science and Engineering, Tongji University, Shanghai 200092, China*
[3]*Laboratory for Ultrafast X-ray and Electron Microscopy, Department of Physics, University of Pavia, Via Agostino Bassi 6, Pavia, PV, 27100, Italy*
[4]*Equal contributors.*
[*]*nabr3523@colorado.edu*

Abstract: We demonstrate temporally multiplexed multibeam ptychography implemented for the first time in the EUV, by using a high harmonic based light source. This allows for simultaneous imaging of different sample areas, or of the same area at different times or incidence angles. Furthermore, we show that this technique is compatible with wavelength multiplexing for multibeam spectroscopic imaging, taking full advantage of the temporal and spectral characteristics of high harmonic light sources. This technique enables increased data throughput using a simple experimental implementation and with high photon efficiency.

1. Introduction

Recent advances in nanofabrication require correspondingly powerful characterization techniques in order to capture both the structure and functional dynamics of nanosystems on their intrinsic length- and time-scales. Exciting new capabilities for probing the structural, mechanical, and transport (charge, heat, spin) properties of materials [1–11] down to angstrom and attosecond scales have been enabled by tabletop coherent short wavelength light sources based on high harmonic generation (HHG). In HHG, an intense femtosecond laser pulse is converted into coherent short-wavelength light, which can span from the vacuum and extreme ultraviolet (VUV and EUV) to the soft x-ray (SXR) spectral regions [12–18]. HHG light sources are characterized by their distinctive temporal and spectral structures — for example, when driven by many-cycle near-infrared laser pulses, HHG radiation emerges as a coherent series of attosecond bursts in the time domain, and as a comb of narrow ($\Delta\lambda/\lambda < 1\%$) harmonics in the spectral domain. Alternatively, when driven either by mid-infrared laser pulses or few-cycle near-infrared pulses, HHG beams emerge as coherent supercontinua [19,20]. These unique properties make it possible to tailor the characteristics of HHG light sources for a wide range of applications in precisely probing the structure and dynamics of molecules, materials and nanosystems.

Coherent short wavelength light produced by HHG light sources has many unique advantages: it can (1) penetrate many visibly-opaque materials, including silicon and certain metallic or oxide layers, to probe and image buried structures; (2) image with nanoscale spatial resolution; (3) access intrinsic elemental, chemical and magnetic contrast, and (4) enable nondestructive

#458955 https://doi.org/10.1364/OE.458955
Journal © 2022 Received 21 Mar 2022; revised 10 Jul 2022; accepted 13 Jul 2022; published 3 Aug 2022

Optics EXPRESS

dynamic imaging, without the need to coat, label or freeze the sample [2,3,8,21]. Lensless microscopy with HHG light sources can be implemented robustly through ptychographic coherent diffractive imaging (CDI) [22–28]. In ptychography, a coherent illuminating probe beam is scanned over an unknown object at a series of overlapping positions to produce a set of diffraction patterns, which are then used in a phase retrieval algorithm to extract a complex-valued image of the sample. Ptychography thus enables robust, diffraction-limited, phase-sensitive imaging of nanosystems. Powerful extensions to ptychography can enable multi-dimensional imaging of functional nanosystems — for example, incorporating a pump-probe scheme into ptychography for ultrafast stroboscopic imaging of nanoscale dynamics [29], scanning the incidence angle to obtain the depth-resolved composition of a specimen [8], or scanning polarization and incidence angle to measure three-dimensional magnetic structures [30,31]. However, the tradeoff between the obtainable field of view and the dataset size and acquisition time inherent to the scanning ptychographic modality is further exacerbated by the introduction of these additional dimensions. Thus, it is extremely desirable to decrease the dataset size and acquisition time necessary for ptychography imaging and its extensions.

Several techniques have recently been developed to enhance the throughput of ptychography. Single-shot ptychography uses a pinhole array and lens to eliminate the scanning requirement [32–35]; however, there is an associated reduction in achievable resolution due to the reduced NA, and the reliance on refractive optics makes it difficult to implement in the EUV or X-ray. An appealing alternative is the use of two spatially separated beams for imaging, here referred to as multibeam imaging, based on ptychographic information multiplexing (PIM) [36]. By illuminating a sample with multiple mutually incoherent modes, multiple images can be simultaneously acquired and reconstructed with no tradeoff in resolution. Multibeam ptychography has been demonstrated to expand the field of view for ptychography microscopes based on visible light sources and synchrotron X-ray beams. With visible light, the requisite mutual incoherence is obtained by using dichroic or polarizing optics to obtain multiple beams differing in color or polarization, respectively [37]. However, such optics are not straightforward to fabricate for EUV wavelengths. PIM with mutually coherent light sources has been demonstrated by using autocorrelation filtering to digitally remove the interference artifacts, however this can only be done in special cases [38]. At synchrotron light sources, multibeam ptychography has been carried out by isolating two areas of a large beam separated by a distance greater than the transverse coherence length [39–41]. However, in addition to being photon-inefficient, this is not a straightforward solution for the fully coherent beams produced by tabletop HHG systems [15]. As such, multibeam ptychography has yet to be implemented for HHG light sources.

In this work, we demonstrate that multibeam ptychography is naturally enabled by the pulsed nature of HHG light sources, which support mutual incoherence of illuminating modes through temporal separation. We demonstrate two-beam ptychographic EUV imaging with increased field of view, and resolution equal to single-mode ptychography with no additional cost in terms of dataset size and collection time. Furthermore, by using a dichroic HHG source and simultaneously acquiring and reconstructing four modes (two wavelength channels in each beam), we show that temporal and spectral multiplexing are mutually compatible, enabling full use of the HHG comb for multi-wavelength imaging. Simultaneous spectral and temporal multiplexing make full use of the unique intrinsic properties of the HHG light source, enabling flux-efficient microscopy with a very simple experiment design. It enables simultaneous acquisition of data at different times, incidence angles, or locations on the sample, and thus can be applied to a wide range of ptychography-based techniques including dynamic imaging [29], ptychotomography [42], and wide-field-of-view imaging [37–41].

Optics EXPRESS

2. Experimental layout

We demonstrate an EUV multibeam ptychography microscope illuminated by a high-harmonic generation (HHG) light source (Fig. 1). Part of the output of a Ti:sapphire amplifier (KMLabs Wyvern HE, $\lambda = 790$ nm, 45 fs pulse duration, 8 mJ pulse energy, 1 kHz repetition rate) is frequency doubled in a β-barium borate (BBO) crystal to generate light at 395 nm, yielding a 2ω pulse energy of 600 μJ when driven by 2 mJ of the fundamental laser. The 2ω beam is then coupled into a 5 cm length, 150 μm diameter hollow core waveguide filled with argon gas to generate harmonics. The driving laser is separated from the generated harmonics by using a 200 nm aluminum filter. This filter also blocks any harmonics with $\lambda > 77$ nm, while harmonics with $\lambda < 39$ nm exceed the HHG cutoff energy for our 400 nm driving laser, and so are not generated. Furthermore, due to the centrosymmetry of the medium, only odd-numbered harmonic orders are emitted. The remaining EUV light thus consists of narrow peaks at the 7^{th} ($\lambda = 56$ nm) and 9^{th} ($\lambda = 44$ nm) harmonics, the ratio of which can be varied by adjusting the argon pressure in the HHG waveguide [43–47]. For temporal multiplexing, we use an argon pressure of approximately 600 torr, to produce a quasi-monochromatic high-harmonic beam with $\lambda = 56$ nm. For wavelength and temporal multiplexing, we use a lower pressure of 150 torr, to produce a bichromatic light source with comparable intensity at $\lambda = 56$ nm and $\lambda = 44$ nm, as shown in the insert of Fig. 1. This beam is focused using a toroidal mirror (gold-coated, $f_{\text{eff}} = 30$ cm, 3x demagnification, 5° incidence angle from grazing), and divided between two paths by a glancing-incidence half-mirror (B_4C coating, fused silica substrate, 3° incidence angle from grazing, nominal reflectivity 95%). The resulting two focusing beams are redirected towards the sample using a pair of glancing incidence recombining mirrors (B_4C coating, fused silica substrate, 3° incidence angle from grazing, nominal reflectivity 95%). The sample is mounted on a precision translation stage ensemble (SmarAct) and translated in the plane perpendicular to the optical axis.

Approximately 1.5 mm in front of the sample, we place a laser-drilled pinhole to introduce a hard edge onto each beam for faster and higher-quality reconstructions. After transmitting through the pinholes, the beams impinge on different areas of the sample separated by about 4 mm, at an angle of ~3° from normal-incidence. This angle is small enough that there is minimal distortion in the diffraction patterns within our detector numerical aperture (NA = 0.27), and hence we do not need to correct for effects from conical diffraction (tilted plane correction) [48,49] during the reconstruction process. The total diffraction pattern is captured by an EUV-CCD detector (Andor iKon-L, 2048×2048, 13.5 μm pixels) positioned about 49 mm after the sample. Although the diffraction orders from the two illuminating beams overlap over the full area of the sensor, the DC peaks ($1/e^2$ intensity width = 135 μm) are separated by about 1.59 mm, or 5.7% of the detector width. This slight separation is helpful in decoupling the contributions from the two beams during the reconstruction process (see Section 6.2).

Optics EXPRESS

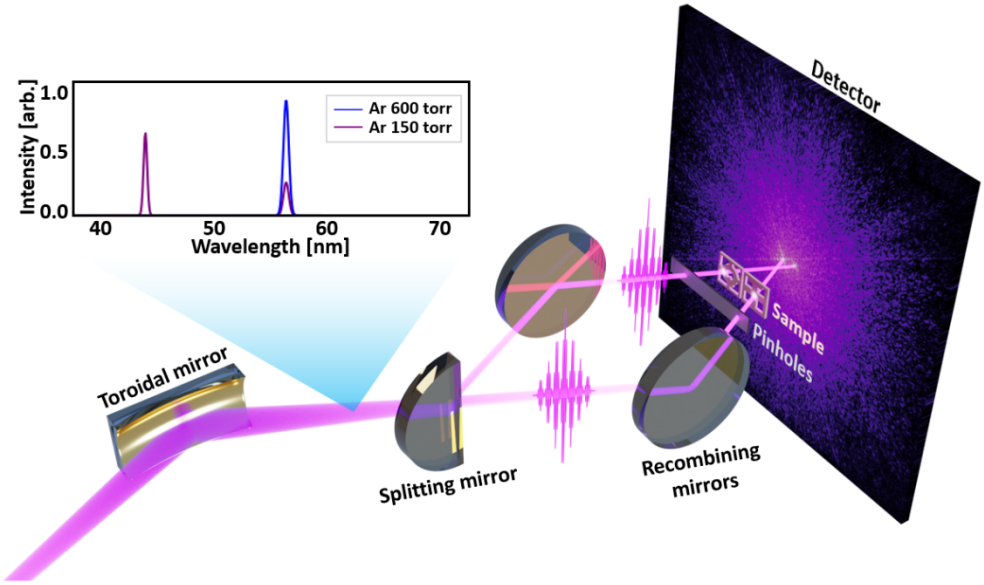

Fig. 1. Schematic of the temporally multiplexed EUV microscope. The output of an HHG light source is divided into two separate paths and focused onto distinct areas of a sample, and the combined diffraction is recorded. Due to differences in the path lengths of the two beams relative to the extremely short duration of the HHG pulse train, the component diffraction patterns add incoherently, and the data can be directly used for multimode ptychography reconstructions. The insert shows the estimated spectra of the EUV light source. By adjusting the argon gas pressure in the waveguide, the generating conditions can be adjusted to select either a single harmonic peak at 56 nm, or two peaks at 44 nm and 56 nm.

3. Temporal multiplexing

In order to implement multiplexing in ptychography, we require that the beams are mutually incoherent, i.e., that they do not interfere. Despite the fact that the two beams in the experiment are derived from the same spatially coherent light source, and thus carry nearly identical spectral content and polarization, no interference is observed in the detector plane between the two component diffraction patterns. This is due to the short-pulse nature of HHG, combined with a slight difference in path length traversed by the two beams. As a field-driven process, the HHG pulse train is emitted during the high-intensity portion of the driving laser pulse. For ~50 fs driving laser pulses, the HHG pulse train has a total envelope duration of ~10 fs [50,51], which gives a longitudinal coherence length of ~10 µm. Because the constituent beams travel optical paths which differ by greater than this very short coherence length, the pulse trains arrive at different times in the detector plane and not interfere. Mathematically, the total electric field of the two HHG beams $E(t)$ is composed of two electric field components $E_a(t)$ and $E_b(t)$. Because the camera exposure time is orders of magnitude longer than the oscillation period of the electric field components, the observed time-integrated diffraction pattern I is

$$\begin{aligned} I &= \int_{-\infty}^{\infty} |E(t)|^2 dt = \int_{-\infty}^{\infty} |E_a(t) + E_b(t)|^2 dt \\ &= \int_{-\infty}^{\infty} |E_a(t)|^2 dt + \int_{-\infty}^{\infty} |E_b(t)|^2 dt + \int_{-\infty}^{\infty} E_a^*(t) E_b(t) + \int_{-\infty}^{\infty} E_a(t) E_b^*(t) dt. \end{aligned} \tag{1}$$

The final two cross terms represent the interference of the constituent fields, and manifest as modulation on top of the overlapped diffraction patterns, with a spatial frequency dependent on

Optics EXPRESS

the probe wavelength and spacing in the sample plane. Even in the case that this frequency is below the pixel size of the detector (as is the case in our experiment), it is generally aliased to lower frequency modulation which prevents the application of multimode ptychography [38]. If, however, the fields are zero outside of some pulse duration τ, and separated in time by $\Delta t > \tau$ due to differences in optical path lengths, then the cross terms vanish:

$$\begin{aligned} I &= \int_0^{\tau} |E_a(t)|^2 dt + \int_{\Delta t}^{\tau+\Delta t} |E_b(t)|^2 dt \\ &= I_a + I_b \end{aligned} \tag{2}$$

Therefore, the observed quantity is the incoherent sum of the individual diffraction components, and multimode ptychography can be directly used to analyze the data. A similar idea has been incorporated into single shot ptychography [52,53] for imaging of a dynamic sample. Here, we use this temporal multiplexing to achieve multibeam imaging with an HHG light source.

The sample consisted of a pair of 3 mm diameter transmission electron microscopy (TEM) grids mounted side by side. The first was a regular copper grid (62 μm period, 42 μm spacing, 20 μm bar) with a rectangular Quantifoil carbon mesh (part number Q410CS7, 9 μm period, 7 μm spacing, 2 μm bar); the second was a Ted Pella H7 Reference grid with Lacey Carbon support structure (part number 01897, 400 Mesh, 63 μm period, 51 μm spacing, 12 μm bar). On both grids, silver nanowires with a diameter of ~100 nm (Sigma-Aldrich Part #778095-25ML) were dropcast to provide deep sub-micron features. Unique and identifiable areas on both grids (the center of the regular TEM grid, and the letter "Q" on the reference grid) were chosen for illumination so that the ptychography results could be easily compared to optical microscope images.

For the data presented here, we collect diffraction patterns at 145 positions in the shape of a Fermat spiral, with an average nearest-neighbor spacing of 5 μm, or about 30% of the beam radius [54]. At each position, we acquire three diffraction pattern images with exposure times of 0.1, 1, and 10 seconds, and combine them to form a composite high dynamic range (HDR) image in order to increase the signal-to-noise ratio. The two fields of view are then reconstructed simultaneously using the PIM multimode ptychography phase retrieval algorithm [36]. In the reconstruction process, we include a supporting noise mode to improve reconstruction fidelity by accounting for systematic incoherence (see Section 6.1) [21,55], as well as a Fourier-space amplitude limit to help decouple the two physical modes (see Section 6.2).

The multibeam ptychography results are shown in Figs. 2(e) and 2(f), and are compared to images obtained with an optical compound microscope (Olympus BH2-UMA, 50x, NA = 0.70) using bright field, narrow-band illumination (white light transmitted through a short pass filter with cutoff wavelength 400 nm) shown in Figs. 2(a) and 2(b), as well as two separately acquired single-beam ptychography reconstructions shown in Figs. 2(c) and 2(d) (acquired by blocking one of the two HHG beams). The single-beam and multibeam ptychography scan parameters (step size = 5 μm, number of scan positions = 145 corresponding to a field of view ≈ 5500 μm^2, exposure time = 0.1/1/10 s, etc.) are equal — thus the total dataset size and acquisition time to complete both single-beam scans were twice those required for the multibeam scan. In the ptychography images, the phase of the complex electric field is indicated by color (hue), while the amplitude is represented by the brightness (value). The coarse features are consistent between all three sets of images; however, fine features such as the nanowires and lacey carbon mesh are not well-resolved by the optical microscope due to the longer illuminating wavelength. In contrast, these features are much more clearly resolved in both the single-beam and multibeam EUV ptychography reconstructions.

The pixel size of the reconstructed images for our ptychography microscope is given by $\Delta r = \lambda z/Np$, where λ is the wavelength, z the sample-detector distance, N the number of pixels on the detector in the x or y direction, and p the detector pixel size in the x or y direction.

Optics EXPRESS

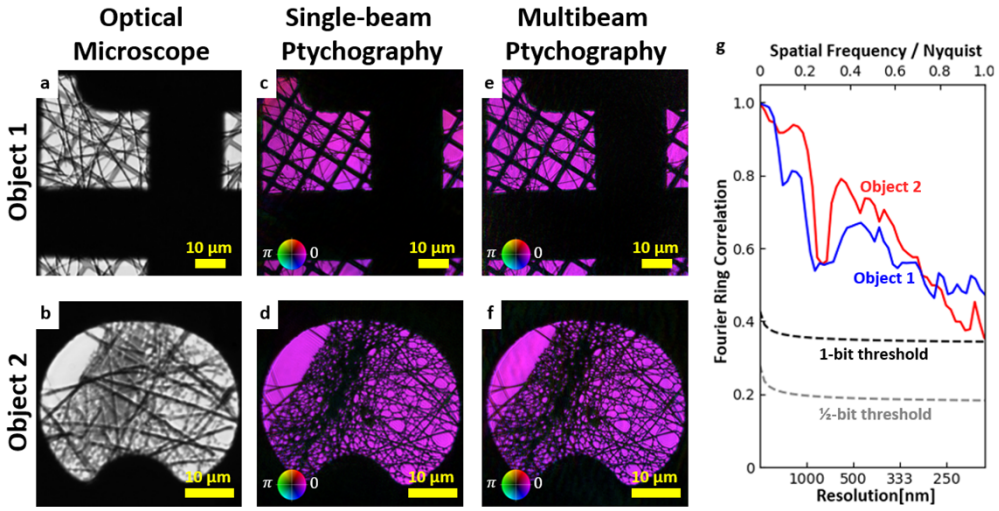

Fig. 2. Single-wavelength, temporally multiplexed ptychography results. **a, b** Optical microscope images with white-light illumination transmitted through a short-pass filter (cutoff wavelength 400 nm) of (**a**, object 1) silver nanorods deposited onto a carbon mesh, and (**b**, object 2) silver nanorods deposited onto a lacey carbon support structure. **c, d** Separately acquired single-mode ptychography reconstructions of the same field of view using 56 nm illumination, and **e, f** simultaneously acquired, temporally multiplexed ptychography reconstructions using 56 nm illumination. **g** Fourier ring correlation measurement for the temporally multiplexed reconstructions, done by separating multibeam scans (**e**, **f**) into two independent data sets and reconstructing separately, demonstrating resolution out to the Nyquist frequency.

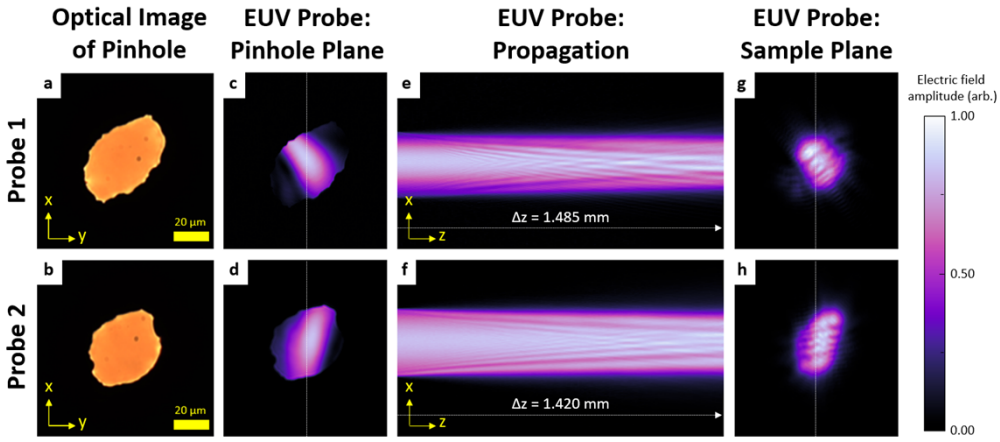

Fig. 3. Characterization of reconstructed probes from multibeam ptychography scans. **a, b** Optical microscope images of the laser-drilled pinholes used to improve and constrain the two illuminating EUV modes for the ptychography microscope. **c, d** Reconstructed probes from the multibeam ptychography in the pinhole plane (**c**, probe 1; **d**, probe 2) **e, f** Evolution of the beams throughout propagation from the pinhole to the sample plane, shown as a slice at y = 0, i.e., the vertical dashed white lines in **c**, **d**, **g** and **h**. **g, h** Reconstructed probes in the sample plane

Optics EXPRESS

For our experimental parameters, $\Delta r \approx 100$ nm. The best achievable resolution for both the single-beam and multibeam reconstructions is given by the Nyquist-Shannon sampling theorem as twice this pixel size, or 200 nm [56]. To quantitatively evaluate the resolution of our images, we split the acquired multibeam dataset into two independent subsets of diffraction patterns, independently reconstructed both subsets, and used Fourier ring correlation (FRC) to measure the repeatability of reconstructed features in diffraction space [57]. The results for both object 1 and 2 are plotted in Fig. 2(g), along with the ½-bit and 1-bit information threshold curves, which represent signal-to-noise ratio levels of 0.5 and 1, respectively, as a function of spatial frequency. The FRC curves for both objects stay above both threshold curves out to the Nyquist frequency corresponding to 200 nm spatial resolution, confirming that we have detectable spatial frequency content above the noise level out to the edge of the detector. This analysis therefore shows that our EUV microscope increases throughput without sacrificing spatial resolution.

The reconstructed probe profiles in the sample plane (Figs. 3(g) and 3(h)) show near-field diffraction features from the hard edge introduced by the pinhole mask. To check the consistency of our results, we numerically backpropagate these probes (Figs. 3(e) and 3(f)) from the sample plane back to the pinhole plane, in which the sharp edge of the aperture is clearly visible without any sort of masking (Figs. 3(c) and 3(d)). This plane is found to be about 1.42 mm and 1.49 mm from the sample for the 1st and 2nd probes, respectively, where the difference in distances is due to a slight relative angle between the pinhole mask and the sample mount. The shapes of the pinholes are confirmed to be correct by comparison with optical microscope images (Figs. 3(a) and 3(b)), giving a high degree of confidence in the accuracy of the retrieved probes and hence the reconstruction quality.

4. Simultaneous temporal and spectral multiplexing

Previous work involving multibeam ptychography employed only a single type of multiplexing; modes with orthogonal polarizations, distinct wavelengths, or different times as described in the previous section, were used to achieve the requisite incoherence. Here, we demonstrate that wavelength-multiplexed spectromicroscopy [58–62] is compatible with temporal multiplexing, and that the two types of multiplexing naturally fit with the characteristics of HHG light sources. We illuminate the same areas of the sample as in the previous section – but now with a bichromatic beam, and acquire a ptychography scan at 300 scan positions arranged in a 20×15 rectangular grid, with average nearest-neighbor spacing of 2 μm and random offset at each position of up to 0.4 μm to avoid gridding artifacts. As in the single-wavelength case, diffraction patterns are acquired at each position with exposure times of 0.1, 1, and 10 seconds, and combined to create HDR data.

To increase the speed of the reconstruction algorithm, we crop the acquired diffraction patterns to 1024×1024 pixels. We then apply the same multimode ptychography algorithm described above with four physical modes to include the two beams, each with two wavelengths, as well as two noise modes, one for each wavelength, for a total of six modes. This produces four images (Figs. 4(a)–4(d)), where each of the objects are reconstructed at the two harmonic wavelengths. Fine features such as edges, nanowires, or lacey carbon appear sharper in the 44 nm images than in their 56 nm counterparts due to the reduced pixel size in the reconstructions. Additionally, there is clear spectral contrast in the lacey carbon film, evident by comparing the same areas of the 56 nm (Fig. 4(e), corresponding to the boxed area in Fig. 4(c)) and 44 nm (Fig. 4(f), corresponding to the boxed area in Fig. 4(d)) reconstructions. In Figs. 4(e)–4(f), the brightness corresponds to the square root of the electric field amplitude to make the intensity and phase contrast clearer. The field transmitted through the thin carbon film has a wavelength-dependent transmission, as well as a positive and wavelength-dependent relative phase shift (Figs. 4(e)–4(f)). By taking the average phase shift over small areas of the carbon film and the open area (orange and white circles, respectively), we find that the measured phase shift is consistent with the

Optics EXPRESS

expected (anomalous) dispersion of an amorphous carbon film [63] of thickness 18–24 nm (Fig. 4(g)), in agreement with thickness estimates from the manufacturer.

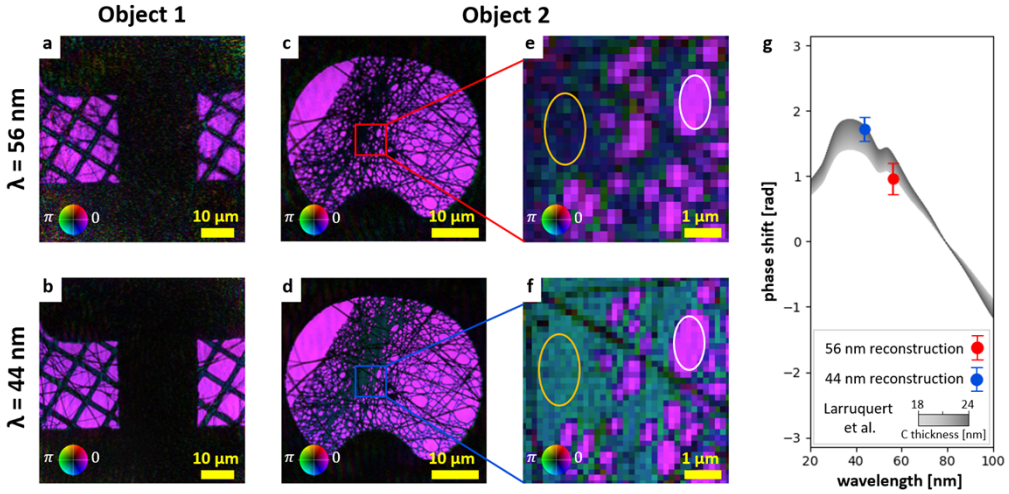

Fig. 4. Temporally and spectrally multiplexed ptychography reconstructions. **a, b, c, d** Simultaneous reconstruction of object 1 (**a,** 56 nm; **b,** 44 nm) and object 2 (**c,** 56 nm; **d,** 44 nm). **e, f** Close-up of object 2 reconstructions, corresponding to the red and blue boxes in **c**, **d**. Here, the brightness corresponds to the square root of the complex field amplitude to highlight the phase and intensity contrast in the lacey carbon support mesh. White and orange ovals correspond to continuous areas of free space and lacey carbon, respectively. **g** Average phase shift measured for the lacey carbon at both harmonic wavelengths, compared to calculations for a range of thicknesses with literature values for the refractive index of amorphous carbon [63].

The set of four reconstructed physical probes in the sample plane (Figs. 5(a)–5(d)) correspond to two beams, each containing two wavelengths. The approximate relative weights of the probes (from which the spectrum in Fig. 1 is estimated) are obtained by setting the free-space regions of the reconstructed objects to a transmission value of unity, and scaling the probe amplitudes appropriately to conserve power. For a given beam, the probe profiles for the 56 nm and 44 nm reconstructions are similar, but not identical. We repeat the procedure of backpropagating the probes to the pinhole plane (Figs. 5(e)–5(h)). As before, we find a well-defined sharp edge for each of the probes which is consistent with the expected pinhole size and shape, thus giving us high confidence in the accuracy of our reconstructed images. By comparing the two harmonic wavelength reconstructions for a given beam in this plane, we observe that the illumination profile on the pinhole is slightly different for the two wavelengths.

Optics EXPRESS

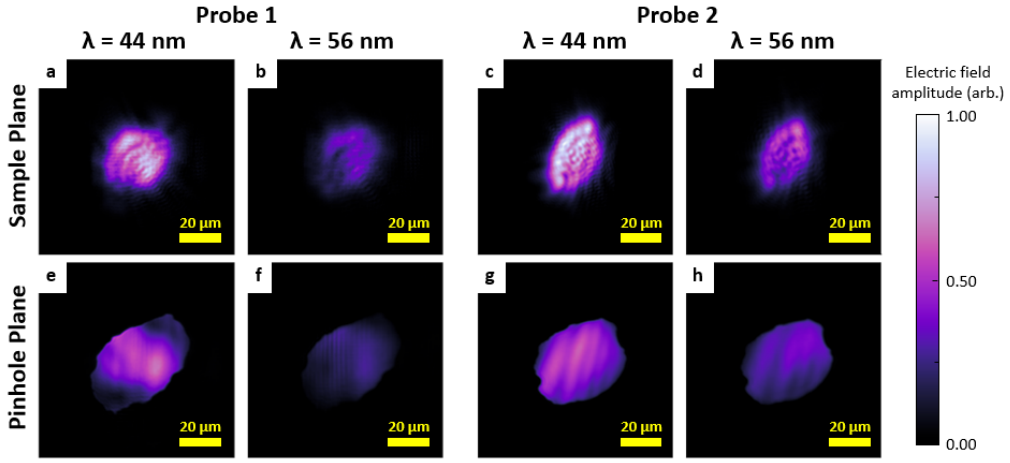

Fig. 5. Reconstructed probes for temporally and spectrally multiplexed ptychography. **a, b, c, d** Probe amplitudes in the sample plane, retrieved as output from the ptychography algorithm. **e, f, g, h** Probe amplitudes in the pinhole plane, obtained by numerical back-propagation from the sample plane. Relative weights of the four probes are obtained by setting the transmission value of the free-space regions of the object reconstruction to unity, and scaling the probes appropriately. The 56 nm reconstructions (**b, d, f, h**) are interpolated onto the same pixel size as the 44 nm reconstructions (**a, c, e, g**).

5. Discussion

We have demonstrated a new type of multiplexed ptychography based on the temporal separation of otherwise similar HHG pulse trains. Mutual incoherence between the illuminating modes, which is necessary for the application of the PIM multimode ptychography algorithm, is acquired effectively automatically due to the very short duration of the HHG pulse train. This technique thus enables multiple diffraction-limited images to be acquired in parallel with an HHG-based microscope without the need for wavelength- or polarization-selective optics, which in the EUV and X-rays are not as readily available as in the visible. We show that this technique can be implemented with a simple, flexible, and photon-efficient experimental design, requiring only a few glancing-incidence optics for division and redirection.

As both illuminating modes have the same polarization and spectral qualities, they can be used to probe the consistent response of a static sample at different spatial positions for large field of view, or at different incidence angles for ptychotomography. Alternatively, a unique capability of the temporal multiplexing would be to acquire simultaneously multiple snapshots of the evolution of a dynamic sample. Thus, we expect that temporally multiplexed ptychography can be used to improve the throughput of a wide range of data-intensive EUV imaging experiments.

Additionally, given the distinctive spectral character of HHG light sources, we show a logical extension by simultaneously incorporating wavelength multiplexing of multiple harmonic teeth for multispectral imaging. This simultaneous implementation of temporal and spectral multiplexing in ptychography is a natural way to utilize the unique properties of HHG light sources. We expect that this technique will continue to work as the number of temporally offset beams is increased through further division and recombination, and as the HHG comb is extended into the soft x-ray region by using ultraviolet driving lasers in multiply-ionized plasmas [45] or mid-infrared necklace beam drivers in helium [64].

Optics EXPRESS

6. Appendix

6.1 Multimode algorithm overview

Ptychographic information multiplexing (PIM) [36] is used in this experiment to simultaneously reconstruct multiple spectral and/or temporal probe and object modes, which are mutually incoherent, from a single ptychographic data set. We use $P_{j,k}(\vec{r})$ and $O_{j,k}(\vec{r})$ to represent these mutually incoherent modes, where j denotes the j^{th} temporally isolated pulsed mode and k the k^{th} spectral mode. Under the projection approximation, the exit surface wave (ESW) in the sample backplane of the j^{th} temporal mode and k^{th} spectral mode at the l^{th} scan position can be modeled as $\psi_{j,\,k,\,l}(\vec{r}) = P_{j,k}(\vec{r}) \cdot O_{j,\,k}(\vec{r} - \vec{r}_l)$, where $\vec{r}$ is the coordinate in object plane and $\overrightarrow{r_l}$ is the position of the l^{th} scan position. The propagation of ESWs from the sample to the detector plane is modeled using the Fresnel diffraction equation, and the expected diffraction intensity pattern recorded by the detector at the l^{th} scan position, $I_l(\vec{q})$, is the incoherent superposition of the individual diffraction patterns from all modes,

$$I_l(\vec{q}) = \sum_{j,\,k} \left|\mathcal{P}_k\{\psi_{j,\,k,\,l}(\vec{r}) \cdot e^{i\vec{r}\cdot\vec{q}_{j,\,k}}\}\right|^2 + \sum_{k} \left|\mathcal{P}_k\{\psi^{noise}{}_{k,\,l}(\vec{r})\}\right|^2 \tag{3}$$

where $\vec{q}$ is the reciprocal space coordinate with respect to the object space coordinate $\vec{r}$. $\mathcal{P}_k\{\psi\} = \mathcal{F}\{\psi \cdot e^{i\theta_k}\}$ is the wavelength-dependent propagator for the k^{th} spectral mode from the sample to the detector plane, where $\mathcal{F}$ is the Fourier transform operation, and $\theta_k = \pi r^2/\lambda_k z$ is the wavelength-dependent phase shift due to the curvature of the wavefronts. In our multibeam ptychography setup, we centered the multiplexing diffraction patterns at the middle point of the centers of all diffraction components. The centers of each diffraction component are off centered in the detector plane, which can be attributed to a linear phase in real space, according to the Fourier shift theorem. One could let the PIM algorithm solve for it as part of the probe phase, but by using this prior knowledge of the imaging system and incorporating a known linear phase into the beam propagator, the PIM algorithm converges faster and achieves higher quality images of samples. We rewrite Eq. (3) below by including the linear phases for each mode in the beam propagator:

$$I_l(\vec{q}) = \sum_{j,\,k} \left|\mathcal{P}_k\{\psi_{j,\,k,\,l}(\vec{r}) \cdot e^{i\vec{r}\cdot\vec{q}_{j,\,k}}\}\right|^2 \tag{4}$$

Furthermore, various experimental uncertainties need to be accounted for to reconstruct high fidelity images, such as illumination pointing and intensity fluctuations, sample vibration, detection noise, etc. They can be modeled as decoherence effects and can be compensated for by including noise modes (Figs. 6(e)–6(f)), which are mutually incoherent with respect to the physical modes (Figs. 6(a)–6(d)) [55]. Here, we included one noise mode, $P^{noise}{}_k(\vec{r})$ and $O^{noise}{}_k(\vec{r})$, for each wavelength in the illumination. The total diffraction intensity pattern at the l^{th} scan position recorded by the detector, $I_l(\vec{q})$, can be expressed as

$$I_l(\vec{q}) = \sum_{j,\,k} \left|\mathcal{P}_k\{\psi_{j,\,k,\,l}(\vec{r}) \cdot e^{i\vec{r}\cdot\vec{q}_{j,\,k}}\}\right|^2 + \sum_{k} \left|\mathcal{P}_k\{\psi^{noise}{}_{k,\,l}(\vec{r})\}\right|^2 \tag{5}$$

where $\psi^{noise}{}_{k,\,l}(\vec{r}) = P^{noise}{}_k(\vec{r}) \cdot O^{noise}{}_k(\vec{r} - \overrightarrow{r_l})$ is the ESW of the noise modes. Notice that there is no linear phase in the propagation of noise modes, because these modes only account for systematic noise.

The PIM algorithm simultaneously reconstructs the complex-valued probe and object modes by iteratively transforming between real and reciprocal spaces and applying constraints in each space. In each iteration, PIM starts from guesses for the physical and noise probe and object modes, calculates the ESW of each mode, $\psi_{j,\,k,\,l}(\vec{r})$ and $\psi^{noise}{}_{k,\,l}(\vec{r})$, and numerically propagates them to the reciprocal space to obtain the diffracted waves,

Optics EXPRESS

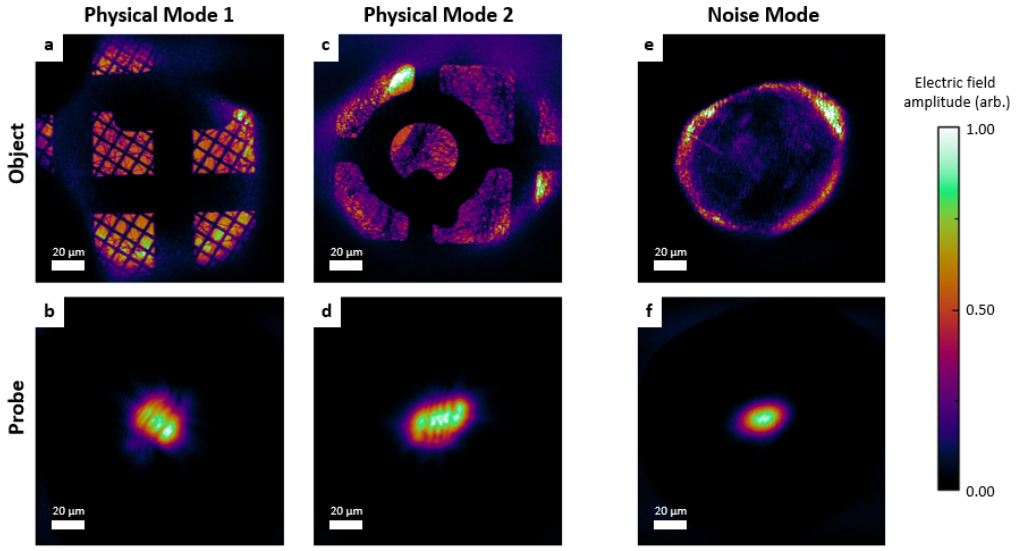

Fig. 6. Physical and noise modes of the temporal multiplexing experiment. **a)** Object 1 reconstruction at 56 nm, **b)** Probe 1 reconstruction, **c)** Object 2 reconstruction, **d)** Probe 2 reconstruction, all shown in amplitude and corresponding to physical modes in the system. **e)** Noise object 1 and **f)** noise probe 1, accounting for decoherence effects in the system.

$\Psi_{j,k,l}(\vec{q}) = \mathcal{P}_k\{\psi_{j,k,l}(\vec{r}) \cdot e^{i\vec{r}\cdot\vec{q}_{j,k}}\}$ and $\Psi^{noise}{}_{k,l}(\vec{q}) = \mathcal{P}_k\{\psi^{noise}{}_{k,l}(\vec{r})\}$. The reciprocal space modulus constraint is applied on these diffracted waves as follows:

$$\Psi'(\vec{q}) = \frac{\sqrt{I^m{}_l(\vec{q})}}{\sqrt{I_l(\vec{q})}} \cdot \Psi(\vec{q}) = \frac{\sqrt{I^m{}_l(\vec{q})}}{\sqrt{\sum_{j,k} |\Psi_{j,k,l}(\vec{q})|^2 + \sum_k |\Psi^{noise}{}_{k,l}(\vec{q})|^2}} \cdot \Psi(\vec{q}) \tag{6}$$

where $I^m{}_l(\vec{q})$ is the measured diffraction pattern at the lth scan position on the detector plane. The updated diffracted waves are then back propagated to the real space to form the updated ESWs, $\psi'_{i,j,k}(\vec{r}) = \mathcal{P}_k{}^{-1}\{\Psi'_{i,j,k}(\vec{q})\} \cdot e^{-i\vec{r}\cdot\vec{q}_{j,k}}$ and $\psi^{noise\prime}{}_{j,k}(\vec{r}) = \mathcal{P}_k{}^{-1}\{\Psi^{noise\prime}{}_{j,k}(\vec{q})\}$, where $\mathcal{P}_k{}^{-1}\{\Psi\} = \mathcal{F}^{-1}\{\Psi\} \cdot e^{-i\theta_k}$ is a backward propagation from the detector to the sample planes. The probe and object functions are updated as follows:

$$P'(\vec{r}) = P(\vec{r}) + \alpha \frac{O^*(\vec{r})}{max(|O(\vec{r})|^2)} \cdot [\psi'(\vec{r}) - \psi(\vec{r})]$$

$$O'(\vec{r}) = O(\vec{r}) + \beta \frac{P^*(\vec{r})}{max(|P(\vec{r})|^2)} \cdot [\psi'(\vec{r}) - \psi(\vec{r})] \tag{7}$$

where α and β are the feedback parameters. This process is performed for every scanning position and repeated until it reaches convergence. With a good probe initialization, we observe good convergence in <1000 iterations. The computer memory usage of the multimode reconstruction is greater in total than that of a single mode reconstruction, but less on a per mode basis as diffraction data, coordinates, etc. are shared between modes.

6.2 Fourier-space amplitude limit to help decouple incoherent modes

An example multibeam diffraction pattern from two mutually incoherent beams is shown in Fig. 7(a). It consists of two single-beam diffraction patterns centered at different positions on the

Optics EXPRESS

detector plane. The PIM algorithm is used to decouple these two single-beam diffraction patterns and reconstruct the corresponding probe and object modes. However, this decoupling process turns out to be very difficult and slow, and can result in crosstalk artifacts appearing as haze or interference fringes in the reconstructed object images, as shown in Figs. 8(b) and 8(d). The origin of these artifacts can be understood by examining the Fourier transform of the PIM reconstructed object 1 and 2, shown in Figs. 8(c) and 8(e). If the two modes have been fully decoupled, the Fourier transform of each object should look similar to single-beam diffraction patterns, with a single bright DC peak in the center. However, the Fourier transforms of both reconstructed objects show an additional residual peak at the position of the other beam (Figs. 8(b) and 8(d)), indicating that there is significant crosstalk between the two modes. We confirm the link between the artifacts in real (object) and reciprocal (diffraction) space by measuring the period of the interference fringe artifacts in the object reconstructions to be 2.2 μm, corresponding exactly to the spacing of the two DC peaks in the diffraction plane (Figs. 8(a)–8(e)).

In order to help decouple these incoherent modes, an additional constraint is applied to the updated diffracted waves in the reciprocal (Fourier) space. During each iteration, at each scan position and for each physical object mode, take the Fourier transform of the updated object function, $\mathcal{P}_k\{O'_{j,k}(\vec{r})\}$, and enforce an amplitude limit of value ε to $|\mathcal{P}_k\{O'_{j,k}(\vec{r})\}|$ in a small area around the DC peak of other object functions (marked by white dashed curve in Fig. 7(b), and blue curves in Figs. 8(c), 8(e), 8(g), 8(i)), i.e. all pixels with value $> \varepsilon$ in this small area are set to ε. The value of ε is initially set to be close to the values of the surrounding pixels in Fourier space, and fine-tuned to improve the reconstruction. This operation is a powerful constraint which greatly helps decouple the two modes. The reconstructed object images with the Fourier-space amplitude limit included are shown in Figs. 8(f)–8(h), showing higher quality and reduced interference artifacts. The Fourier transforms of the object images are shown in Figs. 8(g)–8(i), and show almost no residual crossing diffraction components.

Funding. National Science Foundation (DGE 1650115, DMR 1548924).

Acknowledgments. We thank Carl Sauer for heroic repair work on our EUV CCD. We thank Dr. Kevin Dorney, Dr. Travis Frazer, Dr. Robert Karl Jr, and Dr. Begoña Abad Mayor for helpful discussions.

Disclosures. H.K.: KMLabs Inc. (I, E). M.M.: KMLabs Inc. (I). Other authors declare no conflicts of interest.

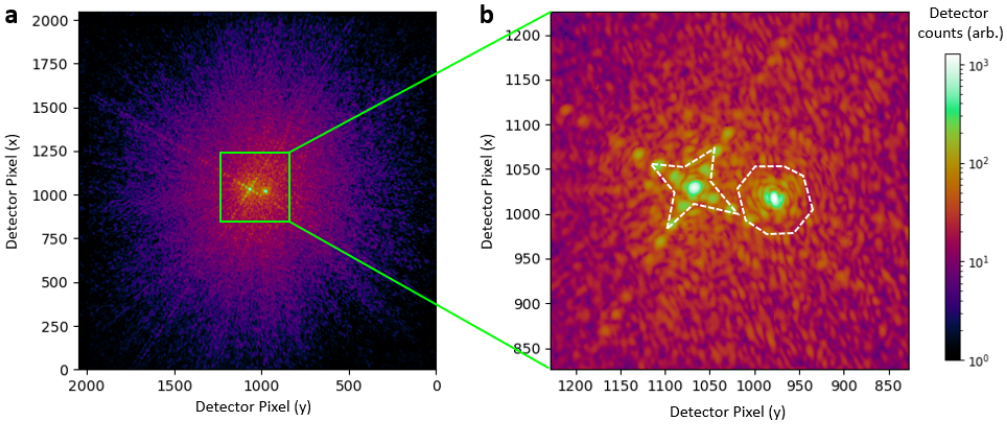

Fig. 7. Diffraction pattern from two temporally incoherent illuminating modes. **a** Full detector area, showing two slightly separated DC peaks with overlapping diffraction orders out to the edges of the detector. **b** Close-up of the central part of the detector. The white dashed curves indicate the areas where the Fourier amplitude limit is applied to help decouple the two probe modes.

Optics EXPRESS

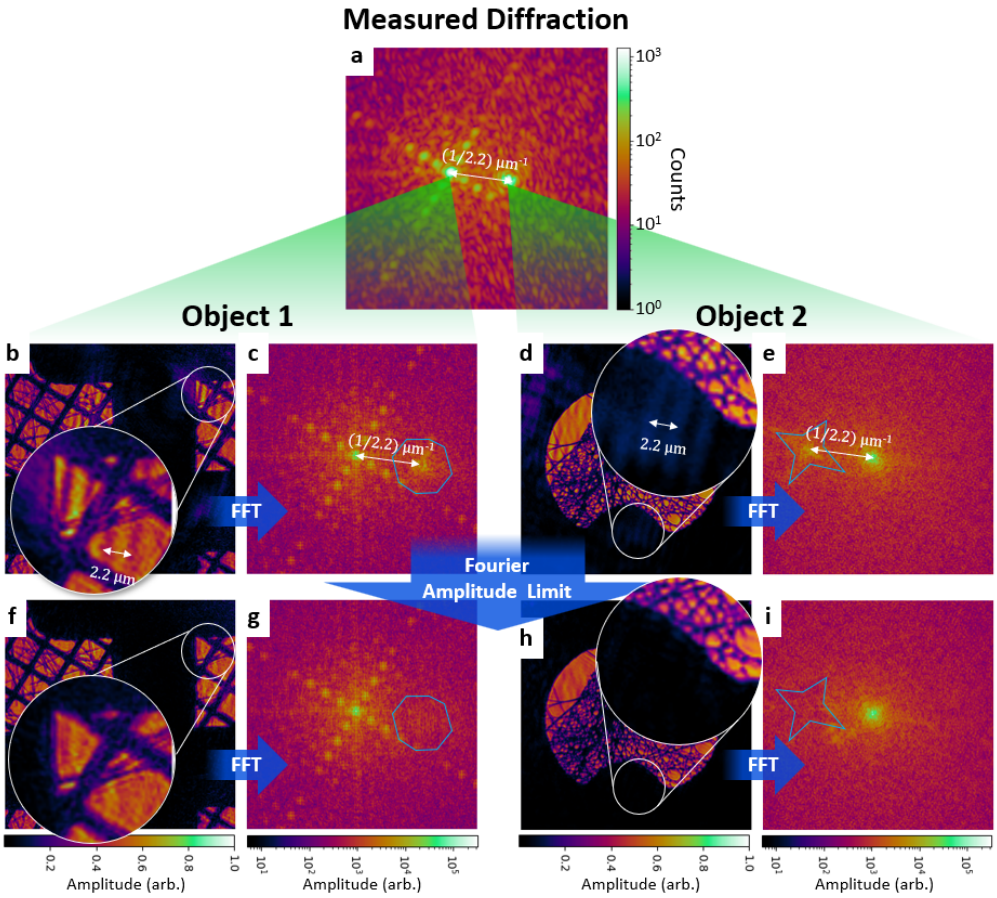

Fig. 8. Application of Fourier amplitude limit operation. **a** Measured diffraction pattern at a single scan position, showing two DC peaks corresponding to two objects. **b** Object 1 reconstruction (without a Fourier amplitude limit operation), and **c** its Fourier transform. Haze and stripe artifacts in **b** object space result from incomplete decoupling of the two modes, visible in **c** Fourier space as residual peaks (inside blue curves). Stripe artifacts in **b** have a period of 2.2 μm, corresponding to the separation distance between the true DC peak and the residual peak in **c** (white arrows). **d, e** similar for Object 2. **f, g, h, i** Reconstructions and Fourier transforms of both objects, this time with the Fourier amplitude limit step applied within the areas of Fourier space encircled by the blue curves.

Optics EXPRESS

Data Availability. Data underlying the results presented in this paper are not publicly available at this time but may be obtained from the authors upon reasonable request.

References

1. C. Chen, Z. Tao, A. Carr, P. Matyba, T. Szilvási, S. Emmerich, M. Piecuch, M. Keller, D. Zusin, S. Eich, M. Rollinger, W. You, S. Mathias, U. Thumm, M. Mavrikakis, M. Aeschlimann, P. M. Oppeneer, H. Kapteyn, and M. Murnane, "Distinguishing attosecond electron-electron scattering and screening in transition metals," Proc. Natl. Acad. Sci. U.S.A. **114**(20), 5300–5305 (2017).
2. O. Kfir, S. Zayko, C. Nolte, M. Sivis, M. Möller, B. Hebler, S. S. Phani, K. Arekapudi, D. Steil, S. Schäfer, M. Albrecht, O. Cohen, S. Mathias, and C. Ropers, "Nanoscale magnetic imaging using circularly polarized high-harmonic radiation," Sci. Adv. **3**(12), eaao464 (2017).
3. D. F. Gardner, M. Tanksalvala, E. R. Shanblatt, X. Zhang, B. R. Galloway, C. L. Porter, R. Karl, C. Bevis, D. E. Adams, H. C. Kapteyn, M. M. Murnane, and G. F. Mancini, "Subwavelength coherent imaging of periodic samples using a 13.5 nm tabletop high-harmonic light source," Nat. Photonics **11**(4), 259–263 (2017).
4. T. D. Frazer, J. L. Knobloch, J. N. Hernández-Charpak, K. M. Hoogeboom-Pot, D. Nardi, S. Yazdi, W. Chao, E. H. Anderson, M. K. Tripp, S. W. King, H. C. Kapteyn, M. M. Murnane, and B. Abad, "Full characterization of ultrathin 5-nm low- k dielectric bilayers: Influence of dopants and surfaces on the mechanical properties," Phys. Rev. Mater. **4**(7), 073603 (2020).
5. P. Tengdin, C. Gentry, A. Blonsky, D. Zusin, M. Gerrity, L. Hellbrück, M. Hofherr, J. Shaw, Y. Kvashnin, E. K. Delczeg-Czirjak, M. Arora, H. Nembach, T. J. Silva, S. Mathias, M. Aeschlimann, H. C. Kapteyn, D. Thonig, K. Koumpouras, O. Eriksson, and M. M. Murnane, "Direct light-induced spin transfer between different elements in a spintronic Heusler material via femtosecond laser excitation," Sci. Adv. **6**(3), eaaz1100 (2020).
6. H. Honarvar, J. L. Knobloch, T. D. Frazer, B. Abad, B. McBennett, M. I. Hussein, H. C. Kapteyn, M. M. Murnane, and J. N. Hernandez-Charpak, "Directional thermal channeling: A phenomenon triggered by tight packing of heat sources," Proc. Natl. Acad. Sci. U.S.A. **118**(40), e2109056118 (2021).
7. A. Beardo, J. L. Knobloch, L. Sendra, J. Bafaluy, T. D. Frazer, W. Chao, J. N. Hernandez-Charpak, H. C. Kapteyn, B. Abad, M. M. Murnane, F. X. Alvarez, and J. Camacho, "A General and Predictive Understanding of Thermal Transport from 1D- And 2D-Confined Nanostructures: Theory and Experiment," ACS Nano **15**(8), 13019–13030 (2021).
8. M. Tanksalvala, C. L. Porter, Y. Esashi, B. Wang, N. W. Jenkins, Z. Zhang, G. P. Miley, J. L. Knobloch, B. McBennett, N. Horiguchi, S. Yazdi, J. Zhou, M. N. Jacobs, C. S. Bevis, R. M. Karl, P. Johnsen, D. Ren, L. Waller, D. E. Adams, S. L. Cousin, C.-T. Liao, J. Miao, M. Gerrity, H. C. Kapteyn, and M. M. Murnane, "Nondestructive, high-resolution, chemically specific 3D nanostructure characterization using phase-sensitive EUV imaging reflectometry," Sci. Adv. **7**(5), eabd9667 (2021).
9. Y. Zhang, X. Shi, M. Guan, W. You, Y. Zhong, T. R. Kafle, Y. Huang, H. Ding, M. Bauer, K. Rossnagel, S. Meng, H. C. Kapteyn, and M. M. Murnane, "Creation of a novel inverted charge density wave state," Struct. Dyn. **9**(1), 014501 (2022).
10. P. D. Baksh, M. Ostrčil, M. Miszczak, C. Pooley, R. T. Chapman, A. S. Wyatt, E. Springate, J. E. Chad, K. Deinhardt, J. G. Frey, and W. S. Brocklesby, "Quantitative and correlative extreme ultraviolet coherent imaging of mouse hippocampal neurons at high resolution," Sci. Adv. **6**(18), eaaz3025 (2020).
11. S. Zayko, O. Kfir, M. Heigl, M. Lohmann, M. Sivis, M. Albrecht, and C. Ropers, "Ultrafast high-harmonic nanoscopy of magnetization dynamics," Nat. Commun. **12**(1), 6337 (2021).
12. P. Tengdin, C. Gentry, A. Blonsky, D. Zusin, M. Gerrity, L. Hellbrück, M. Hofherr, J. Shaw, Y. Kvashnin, E. K. Delczeg-Czirjak, M. Arora, H. Nembach, T. J. Silva, S. Mathias, M. Aeschlimann, H. C. Kapteyn, D. Thonig, K. Koumpouras, O. Eriksson, and M. M. Murnane, "Studies of multiphoton production of vacuum-ultraviolet radiation in the rare gases," J. Opt. Soc. Am. B **4**(4), 595–601 (1987).
13. M. Ferray, A. L. ' Huillier, X. F. Li, L. A. Lomprk, G. Mainfray, and C. Manus, "Multiple-harmonic conversion of 1988 nm radiation in rare gases," J. Phys. B: At. Mol. Opt. Phys. **21**(3), L31–L35 (1988).
14. A. Rundquist, C. G. Durfee, Z. Chang, C. Herne, S. Backus, M. M. Murnane, and H. C. Kapteyn, "Phase-Matched Generation of Coherent Soft X-rays," Science **280**(5368), 1412–1415 (1998).
15. R. A. Bartels, A. Paul, H. Green, H. C. Kapteyn, M. M. Murnane, S. Backus, I. P. Christov, Y. Liu, D. Attwood, and C. Jacobsen, "Generation of Spatially Coherent Light at Extreme Ultraviolet Wavelengths," Science **297**(5580), 376–378 (2002).
16. P. Agostini and L. F. DiMauro, "The physics of attosecond light pulses," Rep. Prog. Phys. **67**(6), 813–855 (2004).
17. T. Popmintchev, M. C. Chen, P. Arpin, M. M. Murnane, and H. C. Kapteyn, "The attosecond nonlinear optics of bright coherent X-ray generation," Nat. Photonics **4**(12), 822–832 (2010).
18. F. Calegari, G. Sansone, S. Stagira, C. Vozzi, and M. Nisoli, "Advances in attosecond science," J. Phys. B: At. Mol. Opt. Phys. **49**(6), 062001 (2016).
19. M. C. Chen, P. Arpin, T. Popmintchev, M. Gerrity, B. Zhang, M. Seaberg, D. Popmintchev, M. M. Murnane, and H. C. Kapteyn, "Bright, coherent, ultrafast soft x-ray harmonics spanning the water window from a tabletop light source," Phys. Rev. Lett. **105**(17), 173901 (2010).
20. T. Popmintchev, M.-C. Chen, D. Popmintchev, P. Arpin, S. Brown, S. Ališauskas, G. Andriukaitis, T. Balčiunas, O. D. Mücke, A. Pugzlys, A. Baltuška, B. Shim, S. E. Schrauth, A. Gaeta, C. Hernández-García, L. Plaja, A. Becker, A.

Optics EXPRESS

Jaron-Becker, M. M. Murnane, and H. C. Kapteyn, "Bright Coherent Ultrahigh Harmonics in the keV X-ray Regime from Mid-Infrared Femtosecond Lasers," Science **336**(6086), 1287–1291 (2012).
21. E. R. Shanblatt, C. L. Porter, D. F. Gardner, G. F. Mancini, R. M. Karl, M. D. Tanksalvala, C. S. Bevis, V. H. Vartanian, H. C. Kapteyn, D. E. Adams, and M. M. Murnane, "Quantitative Chemically Specific Coherent Diffractive Imaging of Reactions at Buried Interfaces with Few Nanometer Precision," Nano Lett. **16**(9), 5444–5450 (2016).
22. H. M. L. Faulkner and J. M. Rodenburg, "Movable aperture lensless transmission microscopy: A novel phase retrieval algorithm," Phys. Rev. Lett. **93**(2), 023903 (2004).
23. J. M. Rodenburg, A. C. Hurst, A. G. Cullis, B. R. Dobson, F. Pfeiffer, O. Bunk, C. David, K. Jefimovs, and I. Johnson, "Hard-X-ray lensless imaging of extended objects," Phys. Rev. Lett. **98**(3), 034801 (2007).
24. P. Thibault, M. Dierolf, A. Menzel, O. Bunk, C. David, and F. Pfeiffer, "High-Resolution Scanning X-ray Diffraction Microscopy," Science **321**(5887), 379–382 (2008).
25. A. M. Maiden and J. M. Rodenburg, "An improved ptychographical phase retrieval algorithm for diffractive imaging," Ultramicroscopy **109**(10), 1256–1262 (2009).
26. M. D. Seaberg, B. Zhang, D. F. Gardner, E. R. Shanblatt, M. M. Murnane, H. C. Kapteyn, and D. E. Adams, "Tabletop nanometer extreme ultraviolet imaging in an extended reflection mode using coherent Fresnel ptychography," Optica **1**(1), 39–44 (2014).
27. B. Zhang, D. F. Gardner, M. D. Seaberg, E. R. Shanblatt, H. C. Kapteyn, M. M. Murnane, and D. E. Adams, "High contrast 3D imaging of surfaces near the wavelength limit using tabletop EUV ptychography," Ultramicroscopy **158**, 98–104 (2015).
28. L. Loetgering, S. Witte, and J. Rothhardt, "Advances in laboratory-scale ptychography using high harmonic sources [Invited]," Opt. Express **30**(3), 4133–4164 (2022).
29. R. M. Karl, G. F. Mancini, J. L. Knobloch, T. D. Frazer, J. N. Hernandez-Charpak, B. Abad, D. F. Gardner, E. R. Shanblatt, M. Tanksalvala, C. L. Porter, C. S. Bevis, D. E. Adams, H. C. Kapteyn, and M. M. Murnane, "Full-field imaging of thermal and acoustic dynamics in an individual nanostructure using tabletop high harmonic beams," Sci. Adv. **4**(10), eaau4295 (2018).
30. C. Donnelly, M. Guizar-Sicairos, V. Scagnoli, S. Gliga, M. Holler, J. Raabe, and L. J. Heyderman, "Three-dimensional magnetization structures revealed with X-ray vector nanotomography," Nature **547**(7663), 328–331 (2017).
31. A. Rana, C.-T. Liao, E. Iacocca, J. Zou, M. Pham, E.-E. C. Subramanian, Y. H. Lo, S. A. Ryan, X. Lu, C. S. Bevis, R. M. Karl, A. J. Glaid, Y.-S. Yu, P. Mahale, D. A. Shapiro, S. Yazdi, T. E. Mallouk, S. J. Osher, H. C. Kapteyn, V. H. Crespi, J. v Badding, Y. Tserkovnyak, M. M. Murnane, and J. Miao, "Direct observation of 3D topological spin textures and their interactions using soft x-ray vector ptychography," arXiv:2104.12933 (2021).
32. X. Pan, C. Liu, and J. Zhu, "Single shot ptychographical iterative engine based on multi-beam illumination," Appl. Phys. Lett. **103**(17), 171105 (2013).
33. P. Sidorenko and O. Cohen, "Single-shot ptychography," Optica **3**(1), 9–14 (2016).
34. D. Goldberger, J. Barolak, C. G. Durfee, and D. E. Adams, "Three-Dimensional Single-Shot Ptychography," Opt. Express **28**(13), 18887–18898 (2020).
35. J. Barolak, D. Goldberger, J. Squier, Y. Bellouard, C. Durfee, and D. Adams, "Wavelength-multiplexed single-shot ptychography," Ultramicroscopy **233**, 113418 (2022).
36. D. J. Batey, D. Claus, and J. M. Rodenburg, "Information multiplexing in ptychography," Ultramicroscopy **138**, 13–21 (2014).
37. R. Karl, C. Bevis, R. Lopez-Rios, J. Reichanadter, D. Gardner, C. Porter, E. Shanblatt, M. Tanksalvala, G. F. Mancini, M. Murnane, H. Kapteyn, and D. Adams, "Spatial, spectral, and polarization multiplexed ptychography," Opt. Express **23**(23), 30250–30258 (2015).
38. C. Bevis, R. Karl, J. Reichanadter, D. F. Gardner, C. Porter, E. Shanblatt, M. Tanksalvala, G. F. Mancini, H. Kapteyn, M. Murnane, and D. Adams, "Multiple beam ptychography for large field-of-view, high throughput, quantitative phase contrast imaging," Ultramicroscopy **184**, 164–171 (2018).
39. M. Hirose, T. Higashino, N. Ishiguro, and Y. Takahashi, "Multibeam ptychography with synchrotron hard X-rays," Opt. Express **28**(2), 1216–1224 (2020).
40. Y. Yao, Y. Jiang, J. A. Klug, M. Wojcik, E. R. Maxey, N. S. Sirica, C. Roehrig, Z. Cai, S. Vogt, B. Lai, and J. Deng, "Multi-beam X-ray ptychography for high-throughput coherent diffraction imaging," Sci. Rep. **10**(1), 19550 (2020).
41. F. Wittwer, M. Lyubomirskiy, F. Koch, M. Kahnt, M. Seyrich, J. Garrevoet, C. David, and C. G. Schroer, "Upscaling of multi-beam x-ray ptychography for efficient x-ray microscopy with high resolution and large field of view," Appl. Phys. Lett. **118**(17), 171102 (2021).
42. M. Dierolf, A. Menzel, P. Thibault, P. Schneider, C. M. Kewish, R. Wepf, O. Bunk, and F. Pfeiffer, "Ptychographic X-ray computed tomography at the nanoscale," Nature **467**(7314), 436–439 (2010).
43. A. Rundquist, "Phase-matched generation of coherent, ultrafast x-rays using high harmonics," (1998).
44. A. S. Sandhu, E. Gagnon, A. Paul, I. Thomann, A. Lytle, T. Keep, M. M. Murnane, H. C. Kapteyn, and I. P. Christov, "Generation of sub-optical-cycle, carrier-envelope-phase-insensitive, extreme-uv pulses via nonlinear stabilization in a waveguide," Phys. Rev. A **74**(6), 061803 (2006).
45. D. Popmintchev, C. Hernández-García, F. Dollar, C. Mancuso, J. A. Pérez-Hernández, M.-C. Chen, A. Hankla, X. Gao, B. Shim, A. L. Gaeta, M. Tarazkar, D. A. Romanov, R. J. Levis, J. A. Gaffney, M. Foord, S. B. Libby, A. Jaron-Becker, A. Becker, L. Plaja, M. M. Murnane, H. C. Kapteyn, and T. Popmintchev, "Ultraviolet surprise: Efficient soft x-ray high-harmonic generation in multiply ionized plasmas," Science **350**(6265), 1225–1231 (2015).

Optics EXPRESS

46. S. Eich, A. Stange, A. v. Carr, J. Urbancic, T. Popmintchev, M. Wiesenmayer, K. Jansen, A. Ruffing, S. Jakobs, T. Rohwer, S. Hellmann, C. Chen, P. Matyba, L. Kipp, K. Rossnagel, M. Bauer, M. M. Murnane, H. C. Kapteyn, S. Mathias, and M. Aeschlimann, "Time- and angle-resolved photoemission spectroscopy with optimized high-harmonic pulses using frequency-doubled Ti:Sapphire lasers," J. Electron Spectrosc. Relat. Phenom. **195**, 231–236 (2014).
47. D. Popmintchev, M.-C. Chen, C. Hernández-García, J. A. Pérez-Hernández, J. Sequeira, S. Brown, F. Dollar, P. Grytchtol, B. Walker, L. Plaja, M. M. Murnane, H. C. Kapteyn, and T. Popmintchev, "Ultrahigh-Efficiency High Harmonic Generation Driven by UV Lasers," in *CLEO 2013 OSA Technical Digest* (2013), p. QW1A.5.
48. D. F. Gardner, B. Zhang, M. D. Seaberg, L. S. Martin, D. E. Adams, F. Salmassi, E. Gullikson, H. Kapteyn, and M. Murnane, "High numerical aperture reflection mode coherent diffraction microscopy using off-axis apertured illumination," Opt. Express **20**(17), 19050–19059 (2012).
49. C. L. Porter, M. Tanksalvala, M. Gerrity, G. Miley, X. Zhang, C. Bevis, E. Shanblatt, R. Karl, M. M. Murnane, D. E. Adams, and H. C. Kapteyn, "General-purpose, wide field-of-view reflection imaging with a tabletop 13 nm light source," Optica **4**(12), 1552–1557 (2017).
50. L. Miaja-Avila, G. Saathoff, S. Mathias, J. Yin, C. La-o-Vorakiat, M. Bauer, M. Aeschlimann, M. M. Murnane, and H. C. Kapteyn, "Direct measurement of core-level relaxation dynamics on a surface-adsorbate system," Phys. Rev. Lett. **101**(4), 046101 (2008).
51. H. C. Kapteyn, M. M. Murnane, and I. P. Christov, "Extreme nonlinear optics: Coherent X rays from lasers," Phys. Today **58**(3), 39–46 (2005).
52. P. Sidorenko, O. Lahav, and O. Cohen, "Ptychographic ultrahigh-speed imaging," Opt. Express **25**(10), 10997–11008 (2017).
53. O. Wengrowicz, O. Peleg, B. Loevsky, B. K. Chen, G. I. Haham, U. S. Sainadh, and O. Cohen, "Experimental time-resolved imaging by multiplexed ptychography," Opt. Express **27**(17), 24568–24577 (2019).
54. X. Huang, H. Yan, R. Harder, Y. Hwu, I. K. Robinson, and Y. S. Chu, "Optimization of overlap uniformness for ptychography," Opt. Express **22**(10), 12634–12644 (2014).
55. P. Thibault and A. Menzel, "Reconstructing state mixtures from diffraction measurements," Nature **494**(7435), 68–71 (2013).
56. C. E. Shannon, "Communication in the Presence of Noise," Proc. IRE **37**(1), 10–21 (1949).
57. M. van Heel and M. Schatz, "Fourier shell correlation threshold criteria," J. Struct. Biol. **151**(3), 250–262 (2005).
58. B. Zhang, D. F. Gardner, M. H. Seaberg, E. R. Shanblatt, C. L. Porter, R. Karl, C. A. Mancuso, H. C. Kapteyn, M. M. Murnane, and D. E. Adams, "Ptychographic hyperspectral spectromicroscopy with an extreme ultraviolet high harmonic comb," Opt. Express **24**(16), 18745–18754 (2016).
59. Y. Esashi, C.-T. Liao, B. Wang, N. Brooks, K. M. Dorney, C. Hernández-García, H. Kapteyn, D. Adams, and M. Murnane, "Ptychographic amplitude and phase reconstruction of bichromatic vortex beams," Opt. Express **26**(26), 34007–34015 (2018).
60. A. Rana, J. Zhang, M. Pham, A. Yuan, Y. H. Lo, H. Jiang, S. J. Osher, and J. Miao, "Potential of Attosecond Coherent Diffractive Imaging," Phys. Rev. Lett. **125**(8), 086101 (2020).
61. D. Goldberger, D. Schmidt, J. Barolak, B. Ivanic, C. G. Durfee, and D. E. Adams, "Spatiospectral characterization of ultrafast pulse-beams by multiplexed broadband ptychography," Opt. Express **29**(20), 32474–32490 (2021).
62. L. Loetgering, X. Liu, A. C. C. de Beurs, M. Du, G. Kuijper, K. S. E. Eikema, and S. Witte, "Tailoring spatial entropy in extreme ultraviolet focused beams for multispectral ptychography," Optica **8**(2), 130–138 (2021).
63. J. I. Larruquert, L. v, R.-d. Marcos, J. A. Méndez, P. J. Martin, and A. Bendavid, "High reflectance ta-C coatings in the extreme ultraviolet," Opt. Express **21**(23), 27537–27549 (2013).
64. L. Rego, N. J. Brooks, Q. L. D. Nguyen, J. San Román, I. Binnie, L. Plaja, H. C. Kapteyn, M. M. Murnane, and C. Hernández-García, "Necklace-structured high-harmonic generation for low-divergence, soft x-ray harmonic combs with tunable line spacing," Sci. Adv. **8**(5), eabj7380 (2022).